

RESEARCH ARTICLE | FEBRUARY 12 2026

Modeling interfacial electron transfer using path integral molecular dynamics FREE

Yoonjae Park ; Adam P. Willard



J. Chem. Phys. 164, 064119 (2026)

<https://doi.org/10.1063/5.0307179>

CHORUS



View
Online



Export
Citation

Articles You May Be Interested In

Relating Franck-Condon blockade to redox chemistry in the single-particle picture

J. Chem. Phys. (September 2018)

Proton-coupled electron transfer at SOFC electrodes

J. Chem. Phys. (June 2023)

Renormalization of excitonic properties by polar phonons

J. Chem. Phys. (September 2022)



Order now

Zurich
Instruments

Freedom to Innovate.

The New VHFLI 200 MHz Lock-in Amplifier.

Orchestrate pulses, triggers, and acquisition as the hub of your experiment.
Discover more – run every signal analysis tool, simultaneously.

Modeling interfacial electron transfer using path integral molecular dynamics

Cite as: J. Chem. Phys. 164, 064119 (2026); doi: 10.1063/5.0307179

Submitted: 14 October 2025 • Accepted: 29 January 2026 •

Published Online: 12 February 2026



View Online



Export Citation



CrossMark

Yoonjae Park and Adam P. Willard^{a)}

AFFILIATIONS

Department of Chemistry, Massachusetts Institute of Technology, Cambridge, Massachusetts 02139, USA

^{a)}Author to whom correspondence should be addressed: awillard@mit.edu

ABSTRACT

Outer sphere electron transfer rates can be calculated from simulation data by sampling the equilibrium statistics of the vertical energy gap. For this calculation, electron transfer is typically represented as an instantaneous change in the atomic partial charges. In this paper, we present an implementation of this procedure that utilizes an explicit path-integral representation of the transferring electron. We demonstrate our methodology by combining path integral molecular dynamics and Marcus–Hush–Chidsey theory to calculate the rate of electron transfer from a ferrocyanide complex to a constant potential gold electrode. We consider the dependence of this rate on electron transfer distance and applied potential. We find that when the electron is represented explicitly via path integral molecular dynamics, as opposed to implicitly via fixed atomic partial charges, the rates and thermodynamics are more consistent with experimental findings. We then apply our methodology to explore the role of bridging spectator cations in modifying electron transfer rates. We find, once again, that the path integral approach produces specific cation effects that are more consistent with experiment than those in which the transferring electron is represented implicitly.

Published under an exclusive license by AIP Publishing. <https://doi.org/10.1063/5.0307179>

I. INTRODUCTION

In molecular dynamics simulations of outer sphere electron transfer, the transferring electron is often represented implicitly, in terms of its effect on the nuclear partial charges. This approach omits the effects of electronic fluctuations on reaction thermodynamics, solvent reorganization energies, and electron transfer rates. In this paper, we use classical molecular dynamics simulation with a path integral-based representation of a transferring electron to study interfacial electron transfer. By comparing to the standard approach, we find that an explicit representation of the electron yields more accurate predictions for electron transfer rates. We extend our approach to investigate the effects of spectator cations on electron transfer rates. Our results indicate that the observed spectator cation effect, i.e., an increase in electron transfer rate with increasing cation size, is due to the ion's effect on the relative stability of the reduced and oxidized states and not (as often speculated) by its influence on the solvent reorganization energy.

Most electrochemical technologies require the transfer of electrons across the electrode–solution interface. The molecular mechanisms that underlie these electron transfer processes are often poorly understood, which is hindering our ability to optimize device

performance and efficiency. There are two broad categories of interfacial electron transfer processes: the highly coupled inner-sphere electron transfer and the weakly coupled outer-sphere electron transfer. Here, we limit our focus to the latter, in which an electron tunnels between a solvated redox species and an electrode. This type of outer-sphere electron transfer is believed to dominate current flow in a variety of electrochemical systems, particularly under conditions where direct adsorption is limited.^{1–4}

Thermal fluctuations of the interfacial electrostatic environment are known to play a crucial role in facilitating the process of outer-sphere interfacial electron transfer. However, the specific roles that solvent molecules and electrolyte species play in mediating electron transfer events remain experimentally inaccessible. Therefore, our current molecular-level understanding of these processes is primarily derived from a combination of theory, electronic structure calculation, and atomistic simulation.

Marcus's theory provides a general framework for computing the rates of outer-sphere electron transfer processes in condensed-phase systems. Within this framework, thermodynamic parameters, such as the solvent reorganization energy, reaction free energy, and activation energy, can be calculated from the results of equilibrium molecular dynamics simulations of the reactant and product states.

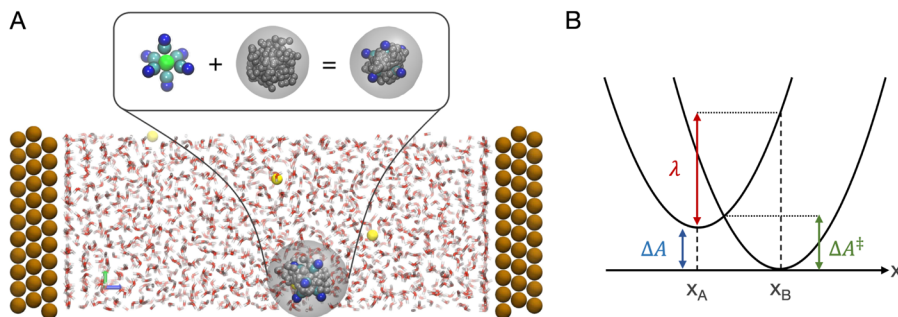


FIG. 1. (a) Snapshot of a molecular dynamics simulation illustrating $[\text{Fe}(\text{CN})_6]^{4-}$ in an aqueous electrochemical cell between two gold electrodes. As the schematic illustrates, the $[\text{Fe}(\text{CN})_6]^{4-}$ comprises a $[\text{Fe}(\text{CN})_6]^{3-}$ complex and an excess ring polymer electron, depicted as a set of gray beads. Atoms shown in red, white, brown, green, cyan, and blue represent O, H, Au, Fe, C, and N, respectively, while yellow atoms correspond to K^+ ions for system charge neutrality. By convention, the z-axis is defined as perpendicular to the electrode surfaces. The gray shaded areas around the electron are visual guides to emphasize the ring polymer representation of the electron. (b) Schematic illustration of Marcus's theory of diabatic free energy surfaces along a reaction coordinate x , defining key quantities involved in electron transfer–reorganization energy (λ), thermodynamic driving force (ΔA), and activation energy (ΔA^\ddagger). We adopt the convention that the forward process proceeds from x_B to x_A , corresponding to a transition from the reduced state to the oxidized state, i.e., $\Delta A = A([\text{Fe}(\text{CN})_6]^{3-}) - A([\text{Fe}(\text{CN})_6]^{4-})$.

More specifically, the statistics of the vertical energy gap, ΔE (i.e., the difference in potential energy between the reactant and product states at fixed nuclear position), are compiled to construct diabatic free energy surfaces—the so-called Marcus parabolas, as illustrated in Fig. 1. This general approach to studying electron transfer processes, therefore, requires (1) an accurate model of the reactant and product states and (2) a robust approach for defining ΔE .

The standard method for meeting these requirements is referred to as the identity exchange (IE) scheme. In this scheme, the reactant and product states are represented by classical point-charge force fields that differ only in the distribution of atomic partial charges. As such, the transferring electron is described implicitly via the specific arrangement of atomic charges. In the earliest implementations of the IE scheme, the entire electron transitions between two ionic centers;^{5,6} however, more recent implementations have distributed the transferring electron charge across an entire molecular complex.^{7,8} While this approach is both straightforward to implement and computationally efficient, it neglects to account for the spatial fluctuations of that transferring electron. The thermodynamic consequences of these fluctuations have not yet been broadly characterized.

Here, we introduce a method for modeling outer-sphere electron transfer in which the electron is described explicitly as a classical ring-polymer. In this method, the molecular system (e.g., everything except for the transferring electron) is modeled with the same basic point-charge force fields that are used in the IE scheme. The ring-polymer electron and the molecular system are co-evolved using standard path integral molecular dynamics (PIMD). Our PIMD scheme allows us to account for the effects of electronic fluctuations in the reorganization energy, reaction free energy, and electron transfer activation energy. While similar PIMD methods have been utilized to evaluate the role of electronic fluctuations in exciton dynamics,^{9–11} polaron physics,^{12,13} and electron trapping in semiconducting materials,¹⁴ they have not yet been applied to study interfacial electron transfer.

The remainder of this paper is organized as follows: In Secs. II and III, we introduce our theoretical and computational methodologies. In Sec. IV, we report and discuss the key properties

of electron transfer computed using both the PIMD and IE schemes, and apply the path integral framework to investigate the influence of bridging cations. Finally, Sec. V provides a summary and concluding remarks.

II. THEORETICAL FRAMEWORK

A. A model of interfacial electron transfer

We consider a molecular system consisting of a redox species in an electrolyte solution confined between a pair of solid constant potential electrodes, such as depicted in Fig. 1(a). The molecular system is coupled to a single *active* electron—modeled as a classical ring polymer—that is capable of transferring between the redox species and the electrodes. Together, the molecular system and the active electron are charge neutral. The dynamics of the molecular system and the electron ring polymer are simulated with classical molecular dynamics, and the resulting trajectories are analyzed in the context of Marcus theory.^{15,16}

Model energetics are described by a three-term Hamiltonian, $\mathcal{H}_{\text{tot}} = \mathcal{H}_{\text{mol}} + \mathcal{H}_e + \mathcal{H}_{\text{int}}$, describing the ring polymer electron, the molecular system, and their interactions, respectively. The molecular system properties are determined by the molecular Hamiltonian,

$$\mathcal{H}_{\text{mol}} = \sum_{i=1}^N \frac{\mathbf{p}_i^2}{2m_i} + U_{\text{mol}}(\{\mathbf{x}^N\}_{\text{mol}}), \quad (1)$$

where \mathbf{p}_i and m_i are the momentum and mass of atom i , $\{\mathbf{x}^N\}_{\text{mol}} = \{\mathbf{x}_1, \mathbf{x}_2, \dots, \mathbf{x}_N\}$ denotes the positions of the N atoms that comprise the molecular system, and U_{mol} is the interaction potential governing all intermolecular interactions, formulated as a classical molecular mechanics force field. The electronic properties are determined by \mathcal{H}_e and \mathcal{H}_{int} , which describe the kinetic and potential energy of the electron, respectively. In particular,

$$\mathcal{H}_e = \frac{\hat{\mathbf{p}}_e^2}{2m_e}, \quad (2)$$

where $\hat{\mathbf{p}}_e$ is the momentum operator of the electron and m_e is the electron mass. The interaction Hamiltonian is given by

$$\mathcal{H}_{\text{int}} = U_{e-\text{mol}}(\hat{\mathbf{x}}_e, \{\mathbf{x}^N\}_{\text{mol}}), \quad (3)$$

where $U_{e-\text{mol}}$ is the interaction potential between the ring-polymer electron and the molecular system and $\hat{\mathbf{x}}_e$ is the position operator of the electron.

B. The electron ring polymer

To capture the quantum mechanical nature of the electron, we adopt a formalism based on the imaginary time path integral.^{17–22} In this formalism, the partition function of the molecular system, \mathcal{Z} , is written as

$$\mathcal{Z} = \int d^{3N} \{\mathbf{x}^N\}_{\text{mol}} e^{-\beta U_{\text{mol}}} \times \mathcal{Z}_e[\{\mathbf{x}^n\}_e], \quad (4)$$

where the partition function of the active electron, \mathcal{Z}_e , is given by

$$\mathcal{Z}_e[\{\mathbf{x}^n\}_e] = \int d^{3n} \{\mathbf{x}^n\}_e e^{-(S_e + S_{\text{int}}) / \hbar}, \quad (5)$$

where $\beta^{-1} = k_B T$, and T , k_B , and \hbar denote the temperature, Boltzmann constant, and reduced Planck's constant, respectively. The parameter n denotes the number of discretized slices along the imaginary time path. The path actions for the electron and its interactions are given by

$$S_e = \int_{\tau=0}^{\beta\hbar} \mathcal{H}_{e,\tau}, \quad S_{\text{int}} = \int_{\tau=0}^{\beta\hbar} \mathcal{H}_{\text{int},\tau}, \quad (6)$$

where the τ -dependent Hamiltonian represents its classical analog at imaginary time τ . For practical implementation, the path action is discretized into n imaginary time slices, such that the quantum particle is equivalently represented as a classical ring polymer composed of n beads linked by harmonic springs.²³ The associated path action of this n -bead ring polymer is given by

$$S_e = \sum_{i=1}^n \frac{m_e n}{2\beta\hbar} (\mathbf{x}_{e,i} - \mathbf{x}_{e,i+1})^2, \quad (7)$$

where $\mathbf{x}_{e,i}$ is the position of the i th bead with $\mathbf{x}_{e,n+1} = \mathbf{x}_{e,1}$. Similarly, S_{int} is determined based on Eq. (3), where the imaginary time path is fully resolved and the resultant action is evaluated as a sum over all imaginary time slices.

The interactions between the electron and the classical nuclei are modeled using a pseudopotential in the form of a truncated Coulomb potential. In particular, the interaction potential between the i th bead of the ring-polymer electron and the j th classical atom in the molecular system is given by

$$U_{\text{el-mol}}^{ij} = \frac{q_i q_j}{4\pi\epsilon_0 n \sqrt{\alpha_j + |\mathbf{x}_{\text{el},i} - \mathbf{x}_j|^2}}, \quad (8)$$

where q and ϵ_0 are the charge and vacuum permittivity, respectively. The pseudopotential parameter, α , is chosen based on the charge and characteristic size of each atom,^{24–26} along with the condition that the electron remains localized around the redox species.

C. Computing diabatic free energy surfaces

Marcus's theory establishes that the canonical reaction coordinate for solution-phase outer-sphere electron transfer is the

vertical energy gap, commonly denoted as ΔE .^{15,16} The vertical energy gap is the instantaneous energy difference between the oxidized and reduced states of the system at fixed nuclear configurations. The diabatic free energy surfaces are related to the equilibrium statistics of ΔE through the foundational relationship, $A(\Delta E) = -k_B T \ln P(\Delta E)$. In a system that obeys linear response, this relationship yields quadratic diabatic free energy surfaces, otherwise known as *Marcus parabolas*, such as illustrated in Fig. 1(b).

We generate diabatic free energy surfaces by sampling the equilibrium statistics of ΔE for configurations originating from the reduced diabatic states. In particular, we sample equilibrium configurations where the electron occupies the redox species, computing $\Delta E = E_{\text{ox}}(\{\mathbf{r}^N\}_{\text{mol}}) - E_{\text{red}}(\{\mathbf{r}^N\}_{\text{mol}})$, where $E_{\text{ox}}(\{\mathbf{r}^N\}_{\text{mol}})$ and $E_{\text{red}}(\{\mathbf{r}^N\}_{\text{mol}})$ are the potential energies of the system in the oxidized and reduced states, respectively, at fixed nuclear configuration, $\{\mathbf{r}^N\}_{\text{mol}}$. More specifically, E_{red} is the total system potential energy when the ring polymer electron occupies the redox species in its original equilibrium configuration, and E_{ox} is the total system potential energy with the electron removed from the simulation and the electrode charges adjusted to restore constant potential. In the latter case, the transferring electron is assumed to equilibrate within the electronic manifold of states within the potentiostatically controlled electrode.

If the equilibrium statistics are Gaussian, then the full free energy profiles can be represented with parabolic fits,

$$A(\Delta E) = \frac{(\Delta E - \langle \Delta E \rangle)^2}{2\sigma^2}, \quad (9)$$

where $\langle \Delta E \rangle$ and σ are the mean and standard deviation of the vertical energy gap distribution. With ΔE as the reaction coordinate, the free energy surface of the oxidized state can be constructed analytically from that of the reduced state (or vice versa). In the linear response case, the curvatures of the oxidized and reduced Marcus parabolas are identical, i.e., $\sigma_{\text{ox}} = \sigma_{\text{red}}$, and their means are related by $\langle \Delta E \rangle_{\text{ox}} = \langle \Delta E \rangle_{\text{red}} - \sigma_{\text{red}}^2 / k_B T$. Consequently, the free energy difference between the two states, identified as the thermodynamic driving force, is expressed as $\Delta A = A_{\text{ox}}(\langle \Delta E \rangle_{\text{ox}}) - A_{\text{red}}(\langle \Delta E \rangle_{\text{red}}) = \langle \Delta E \rangle_{\text{red}} - \sigma_{\text{red}}^2 / (2k_B T)$. The Marcus parabolas allow us to determine two key kinetic parameters: the reorganization energy, $\lambda = \sigma_{\text{red}}^2 / (2k_B T)$, and the activation energy, $\Delta A^\ddagger = (\lambda + \Delta A)^2 / (4\lambda)$.

D. Calculating heterogeneous electron transfer rate constant

Our computational protocol for computing ΔE is illustrated in Fig. 2(a). With this protocol, the net charge difference between the reduced and oxidized states is $-e$ and $+e$ for the electrodes and the anion complex, respectively, which we demonstrate in the supplementary material [Fig. S1(B)].

We base our analysis of interfacial electron transfer kinetics on Marcus–Hush–Chidsey (MHC) theory.^{27–29} This theoretical framework extends classical Marcus theory by incorporating the influence of electrode density of states and Fermi–Dirac statistics, making it well suited for modeling interfacial reactions under electrochemical conditions. At a given overpotential η , the electron transfer rate is given by

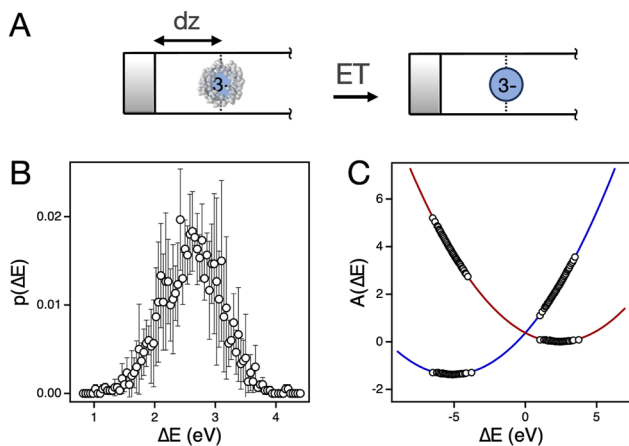


FIG. 2. (a) Schematic illustrating the outer-sphere electron transfer process via the PIMD scheme. In the reduced state (left), the electron occupies the ferricyanide complex, resulting in a total charge of $-4e$, whereas in the oxidized state (right), the electron has merged with the charge distribution of the constant potential electrode. (b) Probability distribution $p(\Delta E)$ with the values of ΔE calculated from reduced state configurations. (c) The representative free energy surfaces $A(\Delta E)$, where the red and blue curves correspond to the parabolic fits for the reduced and oxidized diabatic free energy surfaces, respectively. Symbols denote the statistics derived from simulation data. In panels [(b) and (c)], $dz = 2$ nm, where dz is defined as the shortest distance between the center of mass of the anion complex and the first layer of electrode atoms.

$$k_{\text{MHC}} = \gamma \int_{-\infty}^{\infty} dx \frac{1}{1 + e^{x/k_B T}} \exp \left\{ -\frac{(x - \lambda + e\eta)^2}{4\lambda k_B T} \right\} \quad (10)$$

with

$$\gamma = \frac{|K|^2}{\hbar(4\pi\lambda k_B T)^{1/2}}, \quad (11)$$

where γ is the pre-exponential factor, incorporating the electronic coupling strength K , and the variable of integration, x , represents the energy level of electronic states in the electrode relative to the Fermi level. The overpotential is given by $\eta = V_{\text{ext}} - \Delta A$, where V_{ext} is the applied electrode potential relative to the potential of zero charge. In the limit where the reorganization energy λ is much larger than the thermal energy $k_B T$, the MHC rate expression can be analytically simplified to yield the following expression:

$$k_{\text{MHC}} = \gamma \frac{\sqrt{\pi\lambda'}}{1 + e^{-\eta'}} \text{erfc} \left(\frac{\lambda' - \sqrt{a + \eta'^2}}{2\sqrt{\lambda'}} \right), \quad (12)$$

where $a = 1 + \sqrt{\lambda'}$ and the primed parameters represent the reduced quantities normalized by the thermal energy $k_B T$. This expression captures the probabilistic nature of electron occupancy in the electrode and the thermal broadening of energy levels at finite temperature.

III. COMPUTATIONAL METHODOLOGY

Section II describes our general approach to using PIMD for computing interfacial outer-sphere electron transfer rates. To

demonstrate the utility of this approach, we apply it to study a specific system: the outer-sphere electron transfer from a ferrocyanide complex $[\text{Fe}(\text{CN})_6]^{4-}$ to a gold electrode at the aqueous electrode interface. This well-studied ET reaction serves as a representative system to validate our method and to highlight the effects of electronic fluctuations on the kinetics and thermodynamics of electron transfer.

A. Atomistic simulation details

We perform atomistic molecular dynamics simulations to study heterogeneous electron transfer of ferrocyanide in an aqueous electrochemical cell, as illustrated in Fig. 1(a). The system contains 1658 water molecules, a single $[\text{Fe}(\text{CN})_6]^{4-}$ anion, and 4 K^+ as counterions. The solution is confined between two parallel electrodes aligned in the xy -plane and separated by a distance of 7 nm. The z -axis, therefore, defines the direction perpendicular to the electrode surfaces. Each electrode consists of three layers of atoms arranged in an ideal FCC lattice, with a lattice constant of $d_{\text{Au}} = 4.17$ (consistent with metallic Au) and the 111 facet exposed to the solution. The reduced and oxidized states of the redox species are distinguished based on the location of the ring polymer electron. When the redox species and the electron are spatially separate, the species is considered to be in the oxidized state, i.e., ferricyanide, with a net charge of $-3e$. When the redox species and the electron are co-localized, the species is in the reduced state, i.e., ferrocyanide, with a net charge of $-4e$. The simulation snapshot in Fig. 1 depicts a ferrocyanide configuration. The electron is quantized by $n = 1000$ imaginary time slices, which is large enough to properly describe the behavior of the electron in water, where fictitious masses for the beads are set to 1 amu for computational simplicity.

The dimension of the system is $2.7 \times 2.7 \times 8.0 \text{ nm}^3$, ensuring that the system captures both bulk and interfacial regions,³⁰ and periodic boundary conditions are applied in the x and y directions. For interaction potentials, the SPC/E model is used for water,³¹ and metal electrodes are modeled using parameters developed by Heinz *et al.*³² The Lennard-Jones parameters for the ferricyanide and counterions are adopted from Refs. 7 and 33, which have been shown to accurately reproduce the structures of both the reduced and oxidized states of the anion in an aqueous environment. Pseudopotential parameters (presented in the [supplementary material](#)) for electron-nuclear interactions were chosen based on previous studies to reflect the charge and size of each atom.^{24–26} We validated parameters by comparing the solvation structures of the reduced and oxidized states, quantified by the radial distribution functions, to those presented in Ref. 7. We find satisfactory agreement in the overall structure and excellent agreement on the change in solvation between the oxidized and reduced states. Radial distribution functions are presented in the [supplementary material](#) (Fig. S1). A summary of parameters, including pseudopotentials used in the simulations, is provided in the [supplementary material](#) (Tables S1 and S2).

Simulations were performed with a 1 fs time step. All classical atoms were propagated in the canonical (NVT) ensemble using a Nose-Hoover thermostat to control the temperature, while the beads in the ring-polymer electron, connected by harmonic springs as defined in Eq. (7), were propagated using an NVE integrator combined with a Langevin thermostat. All reported quantities were averaged over 1–3 ns of production simulation following an

initial 0.1 ns equilibration, with configurations output at a frequency of 0.1 ps. We employ the constant potential method³⁴ using the LAMMPS³⁵ ELECTRODE package,³⁶ where the charges of electrode atoms fluctuate in response to the nearby electrostatic environment, resulting in a constant potential between the two electrodes. The positions of the electrode atoms are fixed during the simulations. In addition, the bond lengths and angles of water molecules were constrained using the SHAKE algorithm,³⁷ and long-range electrostatic interactions were treated with the particle-particle particle-mesh algorithm with a real-space cutoff of 13 Å. All simulations were carried out using LAMMPS.

B. A comparative identity exchange scheme

To benchmark and validate our PIMD scheme, we compare our results to the standard IE scheme. In the IE scheme, the oxidized and reduced states differ only in the distribution of atomic point charges (i.e., all other force field parameters are identical), and ΔE is computed by changing the charges at a fixed nuclear configuration. Unlike our PIMD scheme, which explicitly captures the fluctuating effects of quantum delocalization, the IE scheme treats the transitioning electron as a static object. The IE approach has been widely used in classical molecular simulations for computing vertical energy gaps and reorganization energies within the Marcus framework. To facilitate a consistent comparison, the PIMD- and IE-based simulations share an identical set of force field parameters, except for the partial charges on the ferrocyanide complexes. In the IE scheme, ΔE is computed by switching the values of the atomic charges of the ferri- or ferro-cyanide complex at fixed nuclear coordinates. The force field parameters for the IE scheme are specified in Table S3.

IV. RESULTS AND DISCUSSIONS

In this section, we present simulation results focused primarily on calculations of the Marcus–Hush–Chidsey electron transfer rate, k_{MHC} , along with the thermodynamic parameters λ , ΔA , and ΔA^\ddagger , under varying system conditions. We benchmark our results against experiment, when available, although quantitative agreement is not expected due to the highly idealized nature of our simulation setup (e.g., featureless electrodes, non-polarizable solvent, etc.). Despite this, we expect that the general trends we observe are qualitatively reliable. To evaluate the consequences of modeling the transitioning electron explicitly, we compare the results of our PIMD scheme to those generated with an IE scheme carried out on a practically identical system, as described above in Sec. III B. Furthermore, we observe that the spatial distribution of the electron ring polymer in the reduced state (i.e., when it resides on the redox species) is compact and exhibits negligible dependence on the position of the redox species (see the [supplementary material](#) for more details).

A. Dependence of k_{MHC} on electron transfer distance

We analyze the statistics of the vertical energy gap, ΔE , to derive key ET properties—including reorganization energy (λ), activation energy (ΔA^\ddagger), and reaction free energy (ΔA), which are schematically illustrated in Fig. 1(b). To investigate the spatial dependence of electron transfer rate on transfer distance, we present these key properties as a function of the separation distance between the ion

center of the redox complex and the electrode surface, denoted as dz . We find that in all of our simulations, the statistics of ΔE are approximately Gaussian, indicating that the simplifying approximations of Marcus theory (such as discussed in Sec. II C) can be applied to the analysis of our data.

The width of the Marcus parabola exhibits a systematic trend, with $\sigma_{\text{ox}} = \sigma_{\text{red}}$ decreasing as the redox species–electrode separation, dz , decreases. This trend leads to a corresponding trend in the reorganization energy, with λ decreasing as dz decreases. As Fig. 3(a) highlights, this trend is observed for both the PIMD and IE schemes. This shared distance-dependent trend reflects the classical image charge effect, where closer proximity to the electrode stabilizes charge distributions and compresses the energetics,³⁸ confirming that our approach captures the expected electrostatic behavior of ET at the interface.

The dependence of ΔA on dz is plotted in Fig. 3(b). We observe that the two approaches yield similar trends in the dependence of ΔA on dz but differ by nearly 3 eV in value. The PIMD scheme yields values of $\Delta A < 0$, indicating that the oxidized state is more stable, while the IE scheme yields values of $\Delta A > 0$, indicating that the reduced state is more stable. We attribute the difference in ΔA between PIMD and IE to the transferring electron–redox species interaction energy, which is explicitly accounted for in PIMD (via the pseudopotential) and omitted in the IE scheme. This attribution is supported by results presented in the [supplementary material](#), which reveal that the average electron–redox species attachment energy accounts for method-specific differences in the average potential energy difference between the reduced and oxidized states. This electron–redox species attachment energy is analogous to the electron affinity of the oxidized redox species. This same effect is responsible for the difference in ΔE observed between IE and PIMD, as plotted in Fig. 3(c).

We quantify the entropic contribution to electron transfer, ΔS , calculated based on the temperature dependence of the electron transfer free energy, ΔA (via linear fit). This quantity reflects thermodynamic contributions from the ensemble of nuclear configurations that contribute to electron transfer. The dependence of ΔS_{ondz} is plotted in Fig. 3(d). We observe that the variation of ΔS with dz is negligible, and the values obtained from PIMD simulations and the identity exchange scheme are largely consistent with each other. This indicates that entropic effects play only a minor role in the overall driving force and that the electron transfer process is primarily governed by energetic contributions.

The effect of the ET rate on distance can be intuitively understood by considering the effect of dz on the activation energy, ΔA^\ddagger , as plotted in Fig. 3(e). For the IE scheme, the dependence of ΔA^\ddagger on dz is relatively weak, while in contrast, the PIMD results exhibit a more pronounced dz dependence, with ΔA^\ddagger decreasing as the redox center approaches the electrode. This trend indicates that even though the ring-polymer electron remains localized on the redox complex, at closer distances, enhanced electrostatic interactions and interfacial solvent polarization more effectively stabilize the transition state. As our data indicates, this trend is observed across a range of different temperatures.

The values of λ and ΔA combine to yield the Marcus–Hush–Chidsey interfacial ET rate constant, k_{MHC} , as presented in Eq. (12). The resulting dependence of k_{MHC} on dz is plotted in Fig. 3(f). The PIMD scheme predicts rate constants with

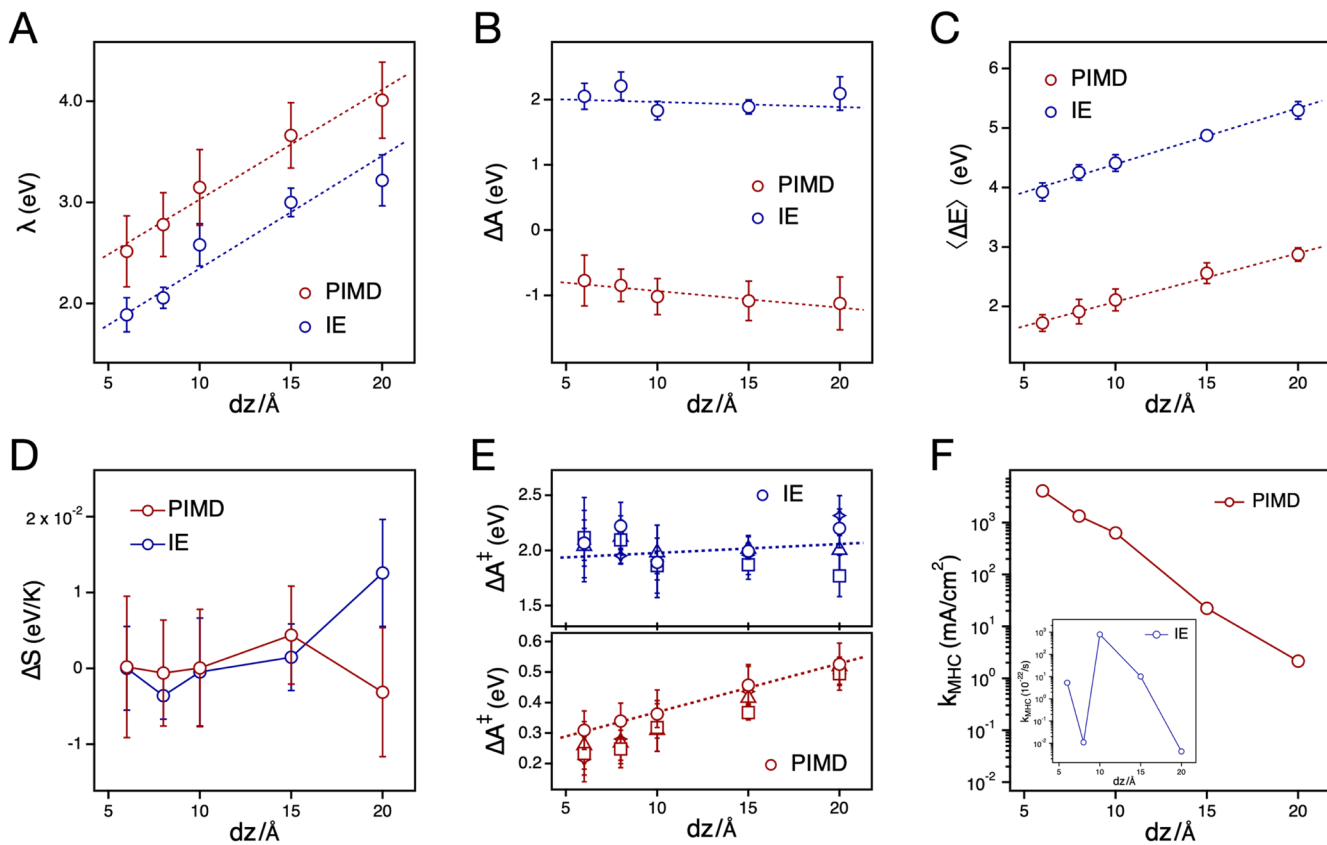


FIG. 3. Dependence of electron transfer properties on transfer distance, dz . In each panel, we compare the results of PIMD- and IE-based sampling schemes, as plotted in red and blue, respectively. (a) Reorganization energy, λ . (b) Electron transfer free energy, ΔA . (c) Mean vertical energy gap ($\langle \Delta E \rangle$). (d) Entropic driving force, ΔS . (e) Activation energy ΔA^\ddagger . For panel (e), different symbols indicate different temperatures: stars (280 K), circles (298 K), triangles (320 K), and squares (340 K). (f) MHC ET rate constants, k_{MHC} , with constant electronic coupling strength $K = 25$ meV. Dotted lines indicate linear fits, and solid lines are guides to the eye.

12 February 2026 17:09:30

a pronounced distance dependence, increasing significantly as the redox species approaches the electrode. The trend in the IE rates (if a trend exists) is difficult to distinguish due to the predicted rate being so close to zero. For the PIMD scheme, we observe that the averaged rate constants at separations near $dz \approx 10\text{\AA}$ are in reasonable agreement with experiment values (~ 300 mA/cm²).^{39,40} This observation suggests (unsurprisingly) that in the physical system, redox current is largely influenced by species located near the electrode, although not necessarily in direct contact with it. We note that since the electronic coupling is assumed to be constant in our analysis, this reported distance dependence is completely due to changes in the thermodynamic parameters λ and ΔA . In contrast, the IE scheme predicts unphysically low rates, effectively vanishing across all distances, with no significant distance dependence. The contrast between the PIMD- and IE-based rate constants highlights a fundamental distinction between the two approaches.

It is worth noting that the largest contribution to the differences in predicted electron transfer rates between the PIMD and IE schemes is the significant offset in ΔA . The energetic interaction between the transferring electron and the redox molecule is explicitly included in the PIMD scheme but omitted in the IE scheme.

The effect of this interaction energy difference can be mitigated by including an artificial shift in the relative energies of the reduced and oxidized states. The [supplementary material](#) includes a calculation of k_{MHC} for both the PIMD and IE methods under conditions where the energetic difference between redox and oxidized states is shifted by a constant to ensure that the average difference is the same between the two schemes and consistent with published values of the redox potential. We find that imposing such a shift yields greater consistency between the PIMD and IE schemes in the predicted electron transfer rates. However, the redox potential-adjusted rates differ qualitatively from experimental predictions, where the predicted rates are approximately 7–8 orders of magnitude larger than those inferred from experiment.

When comparing our simulation results with experimental estimates, we find that the computed reorganization energies tend to slightly overestimate the reported values, yet remain within a physically reasonable range.^{41–43} For the activation barrier, the PIMD results fall closer to experimentally plausible values,^{7,44} reinforcing the validity of the path-integral framework in capturing realistic interfacial ET energetics. This comparison not only reveals the quantitative differences between the two methods but also highlights

scenarios in which the classical IE scheme yields inconsistent or unphysical trends. At the same time, the analysis also identifies properties for which both approaches produce qualitatively similar results, providing insight into when the IE model may offer a reasonable approximation and when a quantum treatment is essential. Overall, our results highlight the potential importance of accounting for the effects of electronic fluctuations in calculations of outer-sphere electron transfer rates.

B. Dependence of ET rate on applied electrode potential

We now examine how the properties that determine k_{MHC} are affected by changes in the applied electrode potential as calculated with the PIMD scheme. To isolate the effects of the electrode potential, we constrain the position of the redox species at $dz = 6\text{\AA}$. We observe that the reorganization energy shows only a modest dependence on the electrode potential, with a general tendency to decrease as the potential increases, as plotted in Fig. 4(a). To further examine this behavior, we also carried out calculations using the IE scheme, which revealed a similarly weak decreasing trend (Fig. S7). This observation is inconsistent with the MHC theory assumption that the reorganization energy is potentially independent. Our results suggest that interfacial electric fields affect solvent structure and dynamics in such a way as to modulate fluctuation amplitudes.

The thermodynamic driving force ΔA [Fig. 4(b)] exhibits a pronounced linear decrease with increasing potential. This trend reflects the downward shift of the Fermi level relative to the redox species at

more positive potentials, which preferentially stabilizes the oxidized state relative to the reduced state. Similarly, the activation energy ΔA^\ddagger decreases nearly linearly with increasing ΔV [Fig. 4(c)], consistent with Marcus theory in the regime where λ varies modestly and ΔA dominates the barrier height.

We observe that the overall electron transfer rate, k_{MHC} , computed via Eq. (12) and plotted in Fig. 4(d), exhibits a significant increase with increasingly applied potential, due primarily to the reduction in activation barrier and enhanced thermodynamic driving force. This behavior aligns with the expected directionality of electron transfer under oxidation bias and further demonstrates that the path integral framework yields physically meaningful rate trends across the electrochemical potential range explored.

C. Influence of bridging cations on interfacial ET

There is ample evidence that the rate of outer sphere interfacial electron transfer is sensitive to the identity of the cation in the supporting electrolyte. However, the physical origin of this *specific cation effect* remains a topic of debate. Some hypothesize that these effects arise through the cations' influence on solvent reorganization energy, λ , e.g., the so-called structure-making and structure-breaking influence on aqueous molecular structure.^{7,45,46} Others hypothesize that cations facilitate electron transfer by bridging the gap between the redox species and the electrode, thereby offering a more favorable tunneling environment for the electron.⁴ Here, we use our PIMD scheme to evaluate these two hypotheses.

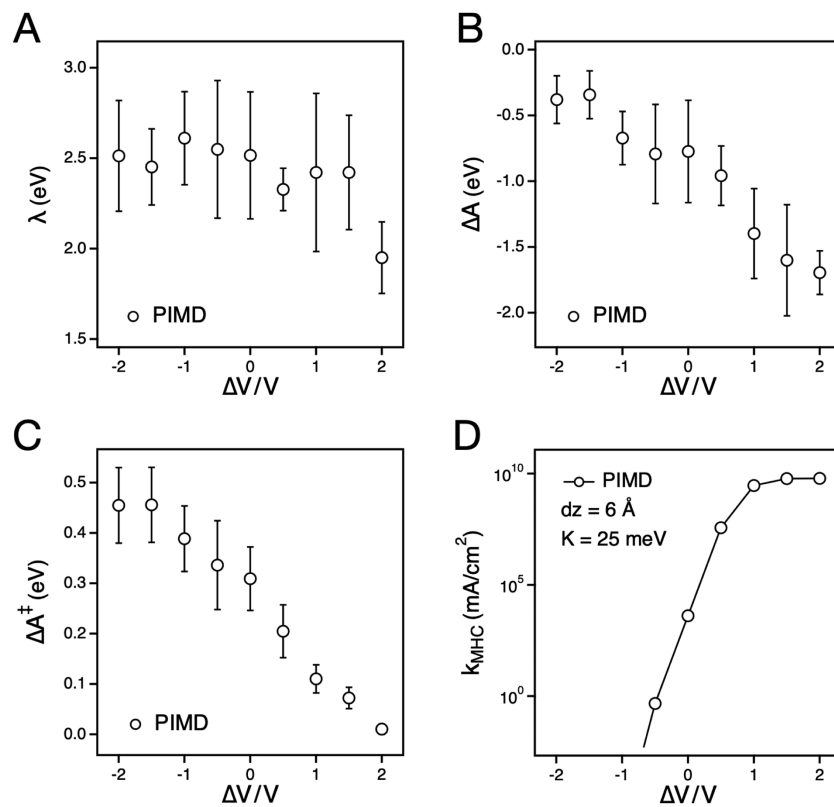


FIG. 4. Response of electron transfer properties to the applied electrode potential ΔV at a fixed anion-electrode separation of $dz = 6\text{\AA}$, computed using path integral molecular dynamics. (a) Reorganization energy λ . (b) Thermodynamic driving force ΔA . (c) Activation energy ΔA^\ddagger . (d) Resulting ET rate constants k_{MHC} .

To investigate the role of cation identity on interfacial electron transfer rate, we carried out simulations in which a cation with a varying ionic radius is constrained to reside between the redox species and the electrode, as illustrated in Fig. 5. In all cases, the redox species is constrained to reside at a distance from the electrode of $d_2 = 8\text{\AA}$. While we did not impose a fixed Fe–cation distance, the designated bridging cation was restricted to remain within the prescribed bridging region, which ensured physically meaningful fluctuations while preserving the intended bridging geometry. Ionic radii were selected to correspond with the series Li^+ , Na^+ , K^+ , Rb^+ , and Cs^+ , and given the dimension of the system and the presence of four cations, the resulting cation concentration is $\sim 0.13 \text{ mol/l}$, as detailed in Sec. III A. The average distance between the Fe atom at the center of the redox complex and the bridging cation (open circles) is shown in Fig. 5(b), computed from both PIMD and IE simulations. Also shown are the average Fe–N distances within the anion complex (filled triangles), pointing to a transition in spatial organization: for small, high charge density cations such as Li^+ , the bridging ion preferentially associates more closely with the redox center, even partially intercalating with the coordinating ligands, whereas for larger cations such as Cs^+ , reduced electrostatic attraction leads to a more peripheral positioning, indicating a weakening of direct interaction with the redox site.

The thermodynamic driving force ΔA , plotted in Fig. 5(a), clearly reflects the transition behavior in bridging the cation position. Among smaller cations, such as Li^+ and Na^+ , ΔA exhibits a steep drop, which indicates a substantial shift in the relative stability of the reduced state of the redox species. As the cation size increases further, the changes in ΔA become more gradual, suggesting that the less strongly bound cations have a smaller influence on the relative stability of the reduced state of the redox species. The influence of cation size is clearly manifested in the thermodynamic driving force ΔA across both PIMD and IE approaches and similarly shapes the activation energy ΔA^\ddagger trends shown in Fig. S8.

The reorganization energy shows relatively weak sensitivity to cation size [Fig. 5(c)]. This insensitivity is somewhat surprising given the pronounced differences in the positioning and stabilization effects described above. One possible explanation for this insensitivity is that there is an interplay of counteracting effects. For example, although Li^+ possesses a higher charge density and would typically be expected to enhance solvent reorganization, its close proximity to the redox complex limits its influence on the surrounding solvent environment. On the other hand, larger cations such as Cs^+ exhibit lower charge density but reside further from the redox center, allowing greater interaction with the surroundings. Such an interplay would align with the view that the primary role

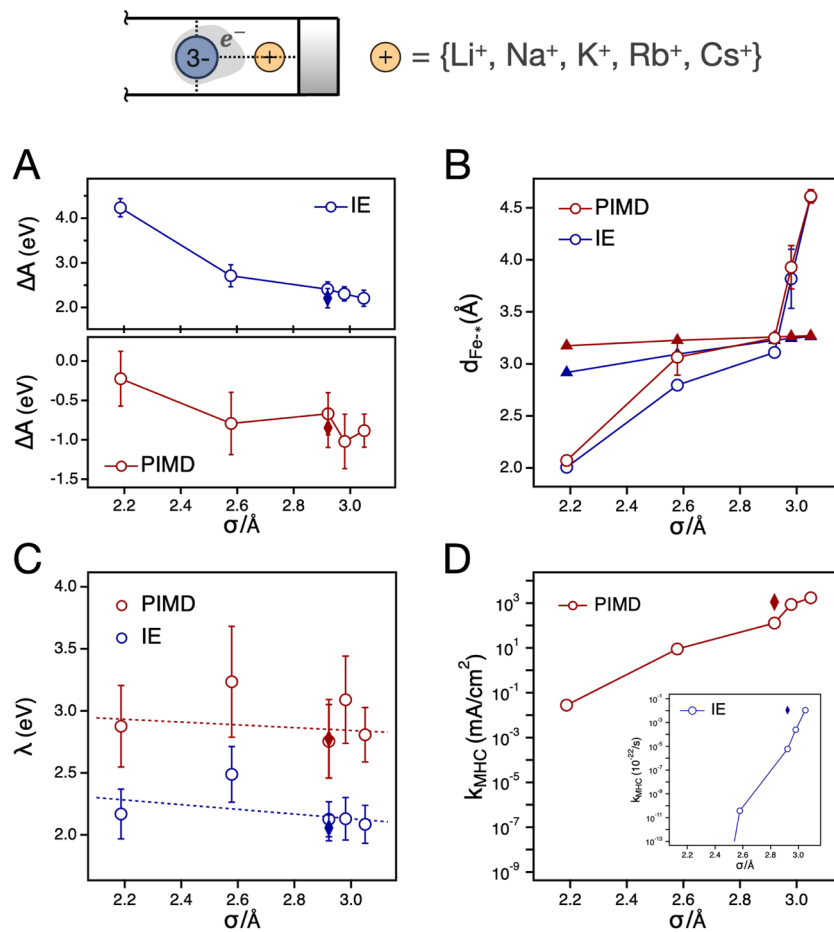


FIG. 5. Effect of bridging cation size on heterogeneous electron transfer properties. Results are shown as a function of cation diameter σ , where the bridging cation is positioned between the redox complex and the electrode surface (top schematic). Red symbols denote the results from PIMD simulations, whereas blue symbols indicate the results from the IE scheme. (a) Thermodynamic driving force ΔA . (b) Distance $d_{\text{Fe}-\text{N}}$ between the Fe atom and bridging cation (open circles) and N atom in redox complex (filled triangles). (c) Reorganization energy λ (d) ET rate constant k_{MHC} . Filled diamond symbols in [(a), (c), and (d)] indicate the results without bridging cation and cation species, including Li^+ , Na^+ , K^+ , Rb^+ , and Cs^+ .

of the bridging cation is to modulate the stabilization of reactant and product states, rather than substantially altering the structural reorganization pathway.^{47,48}

Turning to the resultant ET rate constants k_{MHC} , Fig. 5(d) shows the computed ET rates from both the PIMD and IE schemes. Here, we observe that the ET rates obtained from the PIMD simulations increase markedly with cation size, primarily driven by the more favorable thermodynamic driving forces ΔA associated with larger cations. The rate derived from the IE scheme appears to follow a similar trend; however, the magnitude of the rate is very nearly zero due to the very high predicted activation barrier. In contrast, the IE scheme yields negligibly low rates across all cations due to unrealistically high activation barriers, effectively masking any underlying size-dependent trends. The increasing trend in ET rates with cation size is in qualitative agreement with prior experimental observations.⁷

Finally, to provide a reference for evaluating the bridging cation effect, we include results from a simulation without a bridging cation, marked by filled diamond symbols in each plot of Fig. 5. These reference points correspond to simulations conducted with K^+ and a redox species-electrode separation of $dz = 8 \text{\AA}$, as previously reported in Fig. 3. Interestingly, in the absence of a bridging cation, we observe comparable reorganization energies but slightly more negative thermodynamic driving forces, resulting in higher ET rates. This outcome may stem from stronger direct electrostatic interactions between the redox complex and the electrode, which are otherwise partially screened by the presence of the cation. While these findings suggest that a cation-free interface can, in some cases, enhance ET kinetics, they more broadly highlight the sensitivity of ET behavior to the presence and size of intermediate ions in governing interfacial electron transfer processes.

V. CONCLUSIONS

We have developed and applied a path integral molecular dynamics framework to model electron transfer at electrochemical interfaces, explicitly accounting for the quantum nature of the transferring electron. Using this framework, we construct Marcus parabolas from PIMD simulations to extract key ET properties—including reorganization energy, thermodynamic driving force, and activation energy—aligned with established physical understanding. By comparing this approach with a classical identity-exchange scheme, we demonstrated that the PIMD method provides robust estimates of these quantities, leading to ET rates that better reflect the underlying physics. Furthermore, our analysis of bridging cation effects reveals that the size and spatial positioning of intermediate ions can meaningfully influence ET thermodynamics, while the absence of a bridging cation results in a subtle change in thermodynamic driving force that contributes to a modest enhancement in the ET rate. These findings highlight the utility of the path-integral framework in capturing detailed interfacial behavior and emphasize the importance of explicitly modeling excess electrons when studying ET in complex electrochemical environments beyond classical approximations.

SUPPLEMENTARY MATERIAL

The [supplementary material](#) includes the tables of simulation model parameters that were used in this study and plots establishing model validation.

ACKNOWLEDGMENTS

This work was supported by the U.S. Department of Energy Office of Science, Basic Energy Sciences, under Award No. DE-SC0018094.

AUTHOR DECLARATIONS

Conflict of Interest

The authors have no conflicts to disclose.

Author Contributions

Yoonjae Park: Conceptualization (equal); Data curation (lead); Formal analysis (lead); Investigation (lead); Methodology (lead); Validation (lead); Visualization (lead); Writing – original draft (lead); Writing – review & editing (equal). **Adam P. Willard:** Conceptualization (equal); Supervision (lead); Writing – review & editing (equal).

DATA AVAILABILITY

All data supporting this study are included within the article and its [supplementary material](#).

REFERENCES

- ¹V. Sinha, E. Khramenkova, and E. A. Pidko, *Chem. Sci.* **13**, 3803 (2022).
- ²K. Zhang, Y. Yu, S. Carr, M. Babar, Z. Zhu, B. J. Kim, C. Groschner, N. Khaloo, T. Taniguchi, K. Watanabe, V. Viswanathan, and D. K. Bediako, *ACS Central Sci.* **9**, 1119 (2023).
- ³D.-Q. Liu, M. Kang, D. Perry, C.-H. Chen, G. West, X. Xia, S. Chaudhuri, Z. P. L. Laker, N. R. Wilson, G. N. Meloni, M. M. Melander, R. J. Maurer, and P. R. Unwin, *Nat. Commun.* **12**, 7110 (2021).
- ⁴X. Qin, H. A. Hansen, K. Honkala, and M. M. Melander, *Nat. Commun.* **14**, 7607 (2023).
- ⁵J. Kim, B. M. Savoie, and T. F. Miller, *J. Phys. Chem. C* **125**, 4614 (2021); [arXiv:0804.2891](#).
- ⁶A. P. Willard, S. K. Reed, P. A. Madden, and D. Chandler, *Faraday Discuss.* **141**, 423 (2008); [arXiv:0804.2891](#).
- ⁷B. Huang, K. H. Myint, Y. Wang, Y. Zhang, R. R. Rao, J. Sun, S. Muy, Y. Katayama, J. Corchado Garcia, D. Fragedakis, J. C. Grossman, M. Z. Bazant, K. Xu, A. P. Willard, and Y. Shao-Horn, *J. Phys. Chem. C* **125**, 4397 (2021).
- ⁸A. Tiwari and B. Ensing, *Faraday Discuss.* **195**, 291 (2016).
- ⁹Y. Park, A. Obliger, and D. T. Limmer, *Nano Lett.* **22**, 2398 (2022).
- ¹⁰Y. Park and D. T. Limmer, *J. Chem. Phys.* **157**, 104116 (2022); [arXiv:2205.11780](#).
- ¹¹Y. Park and D. T. Limmer, *Phys. Rev. Mater.* **7**, 106002 (2023).
- ¹²C. G. Bischak, A. B. Wong, E. Lin, D. T. Limmer, P. Yang, and N. S. Ginsberg, *J. Phys. Chem. Lett.* **9**, 3998 (2018).
- ¹³D. T. Limmer and N. S. Ginsberg, *J. Chem. Phys.* **152**, 230901 (2020).
- ¹⁴R. C. Remsing and J. E. Bates, *J. Chem. Phys.* **153**, 121104 (2020); [arXiv:2007.00599](#).
- ¹⁵J. Blumberger and M. Sprak, in *Computer Simulations in Condensed Matter Systems: From Materials to Chemical Biology*, edited by M. Ferrario, G. Ciccotti, and K. Binder (Springer, Berlin, 2006), Vol. 2, pp. 481–506.
- ¹⁶A. M. Limaye, W. Ding, and A. P. Willard, *J. Chem. Phys.* **152**, 114706 (2020).
- ¹⁷D. Chandler and P. G. Wolynes, *J. Chem. Phys.* **74**, 4078 (1981).
- ¹⁸D. M. Ceperley, *Rev. Mod. Phys.* **67**, 279 (1995).
- ¹⁹R. P. Feynman, *Statistical Mechanics* (Westview, 1998).
- ²⁰R. P. Feynman and A. R. Hibbs, *Quantum Mechanics and Path Integrals* (Dover, 2005).
- ²¹A. R. Menzelev, N. Ananth, and T. F. Miller III, *J. Chem. Phys.* **135**, 074106 (2011).

- ²²R. L. Kenion and N. Ananth, *Phys. Chem. Chem. Phys.* **18**, 26117 (2016).
- ²³S. Habershon, D. E. Manolopoulos, T. E. Markland, and T. F. Miller III, *Annu. Rev. Phys. Chem.* **64**, 387 (2013).
- ²⁴M. Parrinello and A. Rahman, *J. Chem. Phys.* **80**, 860 (1984).
- ²⁵J. Schnitker and P. J. Rossky, *J. Chem. Phys.* **86**, 3462 (1987).
- ²⁶R. A. Kuharski, J. S. Bader, D. Chandler, M. Sprik, M. L. Klein, and R. W. Impey, *J. Chem. Phys.* **89**, 3248 (1988).
- ²⁷R. Kurchin and V. Viswanathan, *J. Chem. Phys.* **153**, 134706 (2020); [arXiv:2007.15756](https://arxiv.org/abs/2007.15756).
- ²⁸M. C. Henbridge, E. Laborda, N. V. Rees, and R. G. Compton, *Electrochim. Acta* **84**, 12 (2012).
- ²⁹Y. Zeng, R. B. Smith, P. Bai, and M. Z. Bazant, *J. Electroanal. Chem.* **735**, 77 (2014).
- ³⁰J.-F. Olivier, J. T. Hynes, and D. Laage, *J. Phys. Chem. Lett.* **12**, 4319 (2021).
- ³¹H. J. C. Berendsen, J. R. Grigera, and T. P. Straatsma, *J. Phys. Chem.* **91**, 6269 (1987).
- ³²H. Heinz, R. A. Vaia, B. L. Farmer, and R. R. Naik, *J. Phys. Chem. C* **112**, 17281 (2008).
- ³³G. Prampolini, P. Yu, S. Pizzanelli, I. Cacelli, F. Yang, J. Zhao, and J. Wang, *J. Phys. Chem. B* **118**, 14899 (2014).
- ³⁴J. I. Siepmann and M. Sprik, *J. Chem. Phys.* **102**, 511 (1995).
- ³⁵S. Plimpton, *J. Comput. Phys.* **117**, 1 (1995).
- ³⁶L. J. V. Ahrens-Iwers, M. Janssen, S. R. Tee, and R. H. Meißner, *J. Chem. Phys.* **157**, 084801 (2022); [arXiv:2203.15461](https://arxiv.org/abs/2203.15461).
- ³⁷J.-P. Ryckaert, G. Cicotti, and H. J. C. Berendsen, *J. Comput. Phys.* **23**, 327 (1977).
- ³⁸T. Sometani, *Eur. J. Phys.* **21**, 549 (2000).
- ³⁹T. Pajkossy, *Electrochim. Commun.* **178**, 107969 (2025).
- ⁴⁰T. Pajkossy, M. U. Ceblin, and G. Mészáros, *J. Electroanal. Chem.* **899**, 115655 (2021).
- ⁴¹S. Ghosh, A. V. Soudakov, and S. Hammes-Schiffer, *J. Chem. Theory Comput.* **12**, 2917 (2016).
- ⁴²L. P. Ramírez, A. Boucly, F. Saudrais, F. Bourrel, J.-J. Gallet, E. Maisonneuve, A. R. Milosavljević, C. Nicolas, and F. Rochet, *Phys. Chem. Chem. Phys.* **23**, 16224 (2021).
- ⁴³W. J. Royea, T. W. Hamann, B. S. Brunschwig, and N. S. Lewis, *J. Phys. Chem. B* **110**, 19433 (2006).
- ⁴⁴Y. Kim, D. D. Torres, and P. K. Jain, *Nano Lett.* **16**, 3399 (2016).
- ⁴⁵S. Ringe, E. L. Clark, J. Resasco, A. Walton, B. Seger, A. T. Bell, and K. Chan, *Energy Environ. Sci.* **12**, 3001 (2019).
- ⁴⁶Z.-M. Zhang, T. Wang, Y.-C. Cai, X.-Y. Li, J.-Y. Ye, Y. Zhou, N. Tian, Z.-Y. Zhou, and S.-G. Sun, *Nat. Catal.* **7**, 807 (2024).
- ⁴⁷L. D. Chen, M. Urushihara, K. Chan, and J. K. Nørskov, *ACS Catal.* **6**, 7133 (2016).
- ⁴⁸K. H. Myint, W. Ding, and A. P. Willard, *J. Phys. Chem. B* **125**, 1429 (2021).